PHYSICAL REVIEW B **102**, 094403 (2020)

Noncollinear magnetic modulation of Weyl nodes in ferrimagnetic Mn_3Ga

Cheng-Yi Huang,[1,2] Hugo Aramberri,[2,*] Hsin Lin,[1] and Nicholas Kioussis[2,†]
[1]*Institute of Physics, Academia Sinica, Taipei 11529, Taiwan*
[2]*Department of Physics and Astronomy, California State University, Northridge, California 91330-8268, USA*

(Received 1 April 2020; revised 5 July 2020; accepted 12 August 2020; published 2 September 2020)

The tetragonal ferrimagnetic Mn_3Ga exhibits a wide range of intriguing magnetic properties. Here, we report the emergence of topologically nontrivial nodal lines in the absence of spin-orbit coupling (SOC) which are protected by both mirror and C_{4z}-rotational symmetries. In the presence of SOC, we demonstrate that the doubly degenerate nontrivial crossing points evolve into C_{4z}-protected Weyl nodes with chiral charge of ± 2. Furthermore, we have considered the experimentally reported noncollinear ferrimagnetic structure where the magnetic moment of the Mn_I atom (on the Mn-Ga plane) is tilted by an angle θ with respect to the crystallographic c axis. The evolution of the Weyl nodes with θ reveals that the double Weyl nodes split into a pair of charge-1 Weyl nodes whose separation can be tuned by the magnetic orientation in the noncollinear ferrimagnetic structure.

DOI: 10.1103/PhysRevB.102.094403

I. INTRODUCTION

The discovery of topological states of matter represents a cornerstone of condensed-matter physics that may accelerate the development of quantum information and spintronics and pave the way to realize massless particles, such as Dirac and Weyl fermions. A Weyl semimetal (WSM) is a topological semimetallic material hosting doubly degenerate gapless nodes near the Fermi level in the three-dimensional (3D) momentum space [1–4]. The nodes correspond to effective magnetic monopoles or antimonopoles which carry nonvanishing positive and negative chiral charge $\pm q$. Typically, q takes values of ± 1 corresponding to Weyl nodes, but is also possible to have integers $q = \pm 2, \pm 3, \dots$ for double Weyl nodes, etc. [5] The Weyl nodes give rise to surface states which form open Fermi arcs rather than closed loops.

Compared to their Dirac semimetal counterparts, WSMs require the breakdown either of inversion symmetry or time-reversal symmetry (TRS) to split each fourfold degenerate Dirac node into a pair of Weyl nodes. A number of WSMs that break inversion symmetry have been identified in the past few years [1–4]. Moreover, the presence of crystalline symmetries can further protect multiple Weyl nodes with large chiral charge [6–8]. On the other hand, the discovery of their broken TRS counterparts, which link the two worlds of topology and spintronics, remains challenging and elusive [6]. Many potential TRS-breaking WSMs have been proposed. Recently, three groups have provided unambiguous and direct experimental confirmation that $Co_3Sn_2S_2$ [9,10], which becomes a ferromagnet below 175 K, and Co_2MnGa, a room-temperature ferromagnet [11], are TRS-breaking WSMs. The discovery of magnetic WSMs gives rise to exotic quantum states ranging from quantum anomalous Hall effect to axion insulators [3].

Another remarkable and highly promising class of magnetic materials is the Heusler family [12,13] which includes half metals [14], ferromagnets, ferrimagnets, antiferromagnets, even topological insulators [15,16], and WSMs. In particular, the ferrimagnetic and antiferromagnetic compounds with antiparallel exchange coupling, have recently garnered intense interest because of the faster spin dynamics (in the terahertz range) compared to the gigahertz-range magnetization dynamics of their ferromagnetic counterparts [17].

The Mn_3X ($X =$ Ga, Ge, and Sn) Heusler compounds are considered prototypes with promising applications in the area of spintronics [13,18]. These compounds can be experimentally stabilized in either the hexagonal DO_{19} structure (ϵ phase) or the tetragonal DO_{22} structure (τ phase) [19]. The high-temperature hexagonal crystal structure is antiferromagnetic with a high Néel temperature (∼470 K) and a noncollinear triangular magnetic structure. Recently, several experimental and theoretical studies have demonstrated [20–26] the emergence of large anomalous Hall effect in the noncollinear antiferromagnetic hexagonal Mn_3X family, whose origin lies on the nonvanishing Berry curvature in momentum space. In addition, *ab initio* calculations have revealed that these chiral antiferromagnetic materials are topological WSMs [22]. On the other hand, the low-temperature tetragonal phase, which can be obtained by annealing the hexagonal phase, is ferrimagnetic at room temperature and shows a unique combination of magnetic and electronic properties, including low magnetization [27], high uniaxial anisotropy [28], high spin polarization ($\approx 88\%$) [29–31], low Gilbert damping constant [29], high Curie temperature [32], and large voltage controlled magnetic anisotropy efficiency [33]. Interestingly, neutron-scattering experiments have reported [34] a noncollinear ferrimagnetic magnetic structure in Mn_3Ga where the magnetic moment orientation of the Mn atoms on the Mn-Ga (001) plane is tilted by about 21° with respect to the crystallographic c axis.

---

[*] hugo.aramberri@list.lu
[†] nick.kioussis@csun.edu

2469-9950/2020/102(9)/094403(6)

The objective of this paper is to carry out first-principles electronic structure calculations to investigate the emergence of topological nodal lines in the absence or presence of spin-orbit coupling (SOC) in tetragonal ferrimagnetic Mn_3Ga. Furthermore, we present results of the effect of noncollinear magnetism on the evolution of the Weyl nodes.

II. METHODOLOGY

The electronic structure calculations were carried out by means of first-principles spin-polarized collinear calculations within the density functional theory (DFT) framework as implemented in the VASP package [35]. The Perdew-Burke-Ernzerhof [36] implementation of the generalized gradient approximation (GGA) for the exchange-correlation functional was employed. The plane-wave cutoff energy was set to 400 eV, which was enough to yield well-converged results. The Brillouin zone (BZ) was sampled using a Γ-centered mesh of $10\times10\times10$ k points. The structure was allowed to relax until residual atomic forces became lower than 0.01 eV/Å and residual stresses became smaller than 0.01 GPa. The electron-electron interactions are included where indicated, within the GGA + U approach of Dudarev *et al.* [37]. In this way, the electron correlations are taken into account through a single effective parameter $U_{\text{eff}} = U - J$. The values of U_{eff} for the Mn_I, Mn_{II}, and Ga are set to 2.6 eV, 0, and 0, respectively. Previous studies have shown that these values yield lattice parameters closer to their experimental values [38]. The SOC of the valence electrons is, in turn, included self-consistently using the second-variation method employing the scalar-relativistic eigenfunctions of the valence states [39] as implemented in VASP. Then, DFT-derived wave functions both without and with SOC were, in turn, projected to Wannier functions using the WANNIER90 package [40].

In the DO_{22} structure ($I4/mmm$ space group) the two (001) antiferromagnetically coupled Mn sublattices, shown in Fig. 1(a), consist of Mn_I atoms at the Wyckoff positions $2b$ (0,0,1/2) [Mn_I-Ga (001) plane] and Mn_{II} atoms at the $4d$ (0,1/2,1/4) positions [Mn_{II}-Mn_{II} (001) plane]. For the noncollinear calculation where the magnetic moment of the Mn_I is rotated by an angle π-θ with respect to the [001] direction, the angular dependence of the Wannier Hamiltonian in the presence of SOC is determined from,

$$H(\mathbf{k},\theta) = H_0(\mathbf{k}) + U(\theta)H_{ex}(\mathbf{k})U^{\dagger}(\theta). \qquad (1)$$

Here, $H_0(\mathbf{k})$ is the TRS-preserving Hamiltonian with SOC, $[TH_0(\mathbf{k})T^{-1} = H_0(-\mathbf{k})]$, $H_{ex}(\mathbf{k})$ is the TRS-breaking exchange Hamiltonian, $[TH_{ex}(\mathbf{k})T^{-1} = -H_{ex}(-\mathbf{k})]$, $T = i\sigma_2 K$ is the TRS operator, σ_2 acts on the spin degrees of freedom, K is complex conjugation, $U(\theta) = \exp{(-i\frac{\pi-\theta}{2}\sigma_{2,\text{Mn}_I})}$ is the spin rotation operator, and σ_{2,Mn_I} is the y component of Pauli matrix acting on the spin degrees of freedom of Mn_I.

III. RESULTS AND DISCUSSION

A. Nodal lines in the absence of SOC

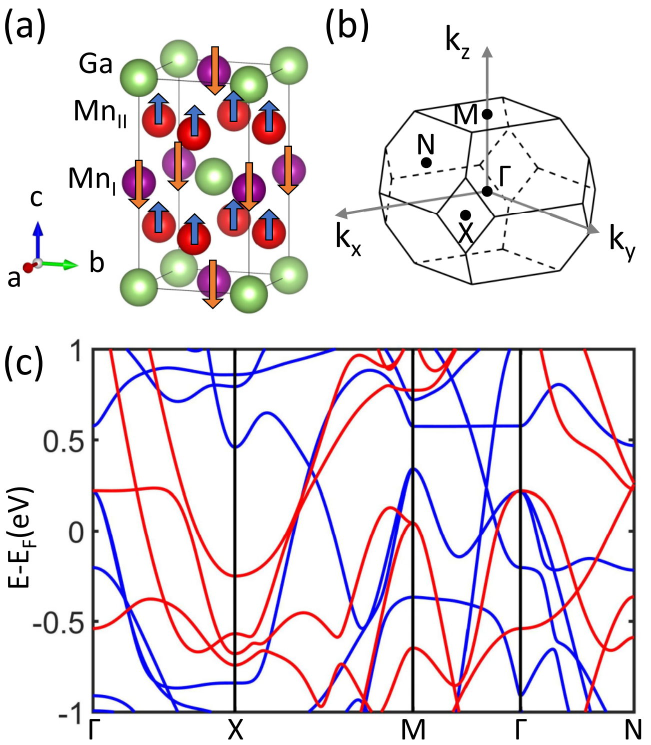

FIG. 1. (a) The tetragonal cell of the DO_{22} ferrimagnetic structure with [001] spin polarization. Arrows denote the magnetic moments of Mn_I (purple) and Mn_{II} (red) sublattices which are coupled antiferromagnetically. (b) The first Brillouin zone of the primitive cell shown in panel (a). (c) Spin-polarized band structure without SOC along the high-symmetry directions of the primitive cell where the spin-up (spin-down) bands are denoted by blue (red).

The calculated lattice parameters $a = b = 3.78$ and $c = 7.08$ Å are in good agreement with previous calculations [34,41,42], which are, however, lower than the experimental values of $a = b = 3.92$ and $c = 7.08$ Å (see Table I). The effect of U on the topology of the band structure is discussed in Sec. III. Overall, our calculated GGA values of the magnetic moments of $-2.83\mu_B$ and $2.30\mu_B$ for the Mn_I and Mn_{II} atoms, respectively, are in good agreement with previous DFT calculations [34,41,42]. Figure 1(c) shows the spin-polarized band structure of the majority- (blue) and minority-spin (red) bands of Mn_3Ga without SOC and with collinear spins along the symmetry lines of the BZ of the primitive cell, shown in Fig. 1(b). For each spin channel, the energy bands can be labeled by the eigenvalues of the crystalline symmetry operator of a particular high-symmetry direction. The band structure along the M-Γ-M direction, shown in Fig. 2(a), features several band crossings close to the Fermi level. Thus, throughout the remainder of the paper, we only focus on the

TABLE I. List of *ab initio* and experimental lattice constants and magnetic moments values for the collinear case. μ_z^{2b} (μ_z^{4d}) denotes the z component of the magnetic moment of the Mn_I (Mn_{II}) atom.

Method	a (Å)	c (Å)	μ_z^{2b} (μ_B/Mn)	μ_z^{4d} (μ_B/Mn)
GGA	3.78	7.08	−2.83	2.30
GGA + U	3.91	7.00	−3.76	2.45
GGA + U + SOC	3.91	7.00	−3.87	2.51
Experiment [34]	3.92	7.08	−3.07	2.08

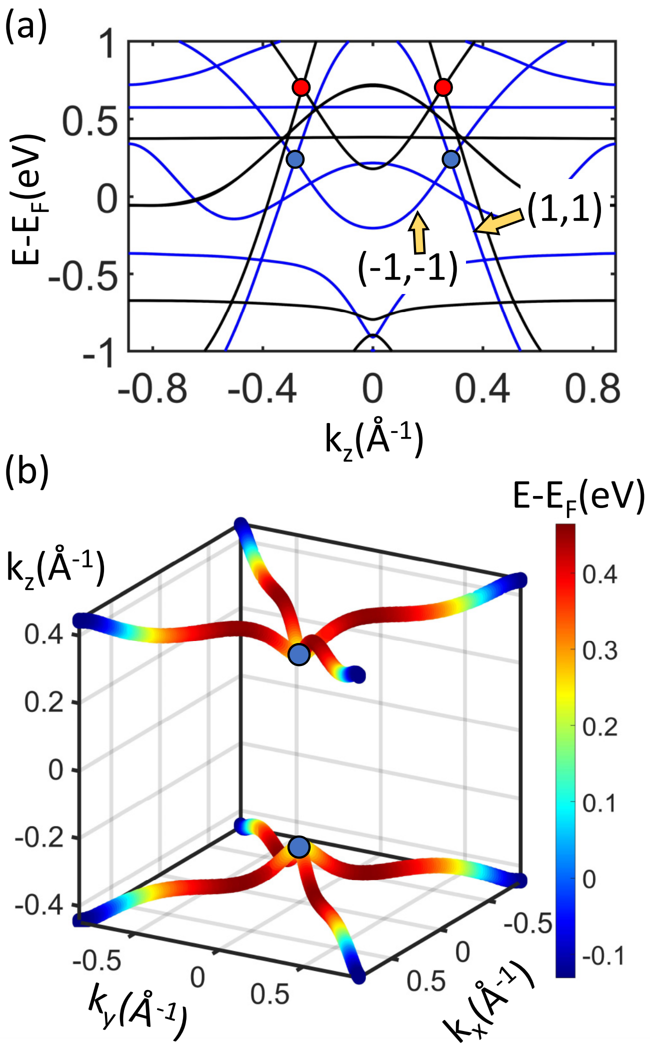

FIG. 2. (a) Spin-polarized band structure along the k_z axis (Γ-M symmetry direction) without SOC, where the blue (black) bands denote the spin-up states calculated from GGA (GGA + U). The two nontrivial crossing points, denoted with the blue dots, are labeled with the pair of eigenvalues ($\pm1, \pm1$) of the mirror $M_{[110]}$ and fourfold rotational C_{4z} symmetries, respectively, which protect them. Red dots denote the nontrivial crossing points when U is turned on. (b) Three-dimensional landscape of the nodal lines where the two blue dots denote the two nontrivial crossing points in (a). The color bar represents the energy of the nodal points relative to the Fermi energy.

crossing points, marked by blue dots in Fig. 2(a), between the majority-spin bands along the k_z (Γ-M) direction. These points are protected by both a mirror reflection symmetry normal to the [110] direction $M_{[110]}$ and a fourfold rotational symmetry C_{4z} and, hence, can be labeled by the pair of eigenvalues ($\pm1, \pm1$) of $M_{[110]}$ and C_{4z}, respectively. The effective kp model in the basis $\{|(1,1)\rangle, |(-1,-1)\rangle\}$ up to the order of k^2 in the absence of SOC can be straightforwardly derived and is given by

$$H_{\mathrm{NL}} = \left(m_1 - m_2 k_z^2\right)s_3 + a\left(k_x^2 - k_y^2\right)s_1, \tag{2}$$

TABLE II. The C_{4z}-protected Weyl fermion on the k_z axis. $u_c(u_v)$ denotes the eigenvalue of C_{4z} in the conduction (valence) band. C denotes the chiral charge.

k_z (Å^{-1})	E-E_F (meV)	u_c/u_v	C	Dispersion on the k_x-k_y plane
0.2811	229	−1	2	k^2
−0.2811	229	−1	−2	k^2

where $\boldsymbol{k}$ is close to the Γ point, $m_1 m_2 > 0$, the s_i's are Pauli matrices, and the nodal lines lie on $k_z = \pm\sqrt{\frac{m_1}{m_2}}$ and $k_x = \pm k_y$. We have tracked the nodal lines on the $M_{[110]}$-invariant plane. The other nodal lines on the $M_{[1\bar{1}0]}$-invariant plane were determined using the C_{4z}-rotational symmetry. Figure 2(b) shows the 3D landscape of nodal lines in momentum space. We find that the nodal lines are topologically nontrivial characterized by the π-Berry phase [43–45]. The two blue points denote the nontrivial crossing points as well as the intersecting points of nodal lines along the k_z direction in Fig. 2(b). Notably, the crossing points remain gapless and robust against a distortion breaking either $M_{[110]}$ or C_{4z}.

B. Weyl nodes in the presence of SOC

In the presence of SOC, the symmetry conservation depends on the magnetic orientation and the crystalline symmetries. More specifically, the [001] collinear magnetic configuration is invariant under: (1) inversion symmetry (P), (2) fourfold rotational symmetry about the z axis (C_{4z}), and (3) mirror reflection symmetry normal to the z direction (M_z). We next discuss the effect of magnetization orientation (collinear versus noncollinear) on the topological features of the band structure.

Weyl nodes in collinear ferrimagnetism. In the presence of SOC, the mirror symmetry $M_{[110]}$ is no longer preserved when the magentization of the collinear ferrimagentic Mn$_3$Ga is along the [001] direction. Consequently, in general, the nodal points in Fig. 2(b) are gapped out except for those crossing points along k_z which are protected by the C_{4z}-rotational symmetry [46]. Thus, for the band structure along the C_{4z}-invariant k_z axis, shown in Fig. 3(a), we can identify the states by the eigenvalues of C_{4z} and locate the nontrivial crossing points associated with different eigenvalues. The nontrivial crossing points, marked by red circles in Fig. 3(a) are Weyl nodes protected by C_{4z} symmetry, whose position along k_z, energy relative to E_F, ratio of conduction- to valence-band C_{4z} eigenvalues u_c/u_v, chiral charge C, and dispersion are summarized in Table II. Interestingly, the C_{4z}-protected Weyl fermion with $u_c/u_v = -1$ carries chiral charge +2 and has quadratic dispersion on the k_x-k_y plane [6], in sharp contrast to the double Weyl fermion with fourfold degeneracy and linear dispersion [1]. Its other parity partner has opposite chiral charge of −2. Based on the above analysis, the effective kp model in the basis of the C_{4z} eigenstates $\{|e^{-i(\pi/4)}\rangle, |e^{i(3\pi/4)}\rangle\}$, up to order of k^2 for the C_{4z}-protected Weyl nodes can be straightforwardly adapted from Ref. [6] and reads

$$H_{\mathrm{WP}} = \left(m_1 - m_2 k_z^2\right)s_3 + \left(ak_+^2 + bk_-^2\right)s_+ + \left(ak_-^2 + bk_+^2\right)s_-, \tag{3}$$

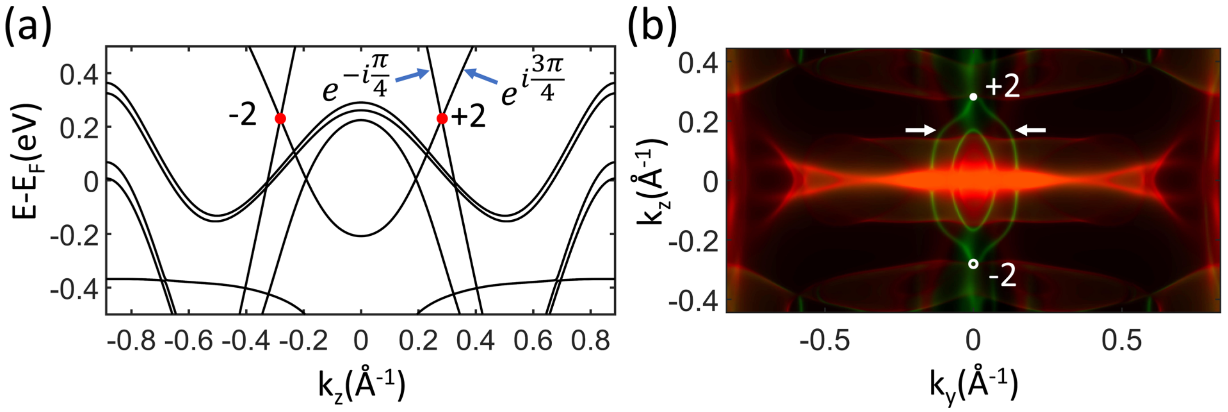

FIG. 3. (a) Band structure along the k_z axis (Γ-M symmetry direction) with SOC, protected by C_{4z} symmetry. The two Weyl points, denoted with red dots, have chiral charges of ± 2. $e^{-i(\pi/4)}$ and $e^{i(3\pi/4)}$ indicate the eigenvalues of C_{4z} for the crossing bands, respectively. (b) Two Fermi arcs on the (100) surface where the green (red) color denotes the spectral weight of the surface (bulk) states. The solid (hollow) white circle denotes positive (negative) chiral charge, and the white arrows indicate the Fermi arcs emerging from the Weyl nodes.

where $\boldsymbol{k}$ is around the Γ point, $k_\pm = k_x \pm ik_y$, $s_\pm = s_1 \pm is_2$, $|a| \neq |b|$, $m_1 m_2 > 0$, and the Weyl node positions are at $k_z = \pm\sqrt{\frac{m_1}{m_2}}$. Interestingly, if $a = b$, H_{WP} reduces to H_{NL} in Eq. (2), implying that the gap opening of the nodal lines would close. Figure 3(b) displays the two Fermi arcs on the (100) surface emerging from the two charge-2 Weyl nodes.

Evolution of Weyl fermions in noncollinear ferrimagnetism. Neutron-scattering experiments have reported [34] a noncollinear ferrimagnetic magnetic structure in the DO$_{22}$ ferrimagnetic Mn$_3$Ga structure where there is a significant in-plane magnetic moment $\mu_x^{2b} = 1.19\mu_B$ carried by the Mn$_I$ atoms [on the Mn-Ga (001) plane] leading to a 21° tilt of the Mn$_I$ moment from the crystallographic c axis [see Fig. 4(a)]. This noncollinear magnetic ordering spontaneously breaks both the C_{4z} and the M_z symmetry operations whereas only preserving P. Consequently, the C_{4z}-protected double Weyl fermion on the k_z axis for the case of collinear ferrimagnetism splits into two charge-1 Weyl fermions which shift away from the k_z axis.

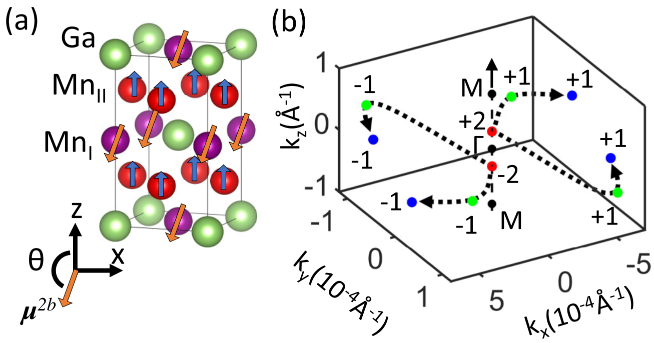

FIG. 4. (a) Noncollinear ferrimagnetic DO$_{22}$ structure of Mn$_3$Ga [34] where the Mn$_I$ atoms [on the Mn-Ga (001) plane] carry a substantial in-plane magnetic moment leading to a tilt of their moments from the crystallographic c axis. (b) Evolution of Weyl nodes in the 3D BZ as a function of tilt angle θ where the red, green, and blue circles denote the Weyl nodes at $\theta = 180°$, 170°, and 160°, respectively. The dashed arrows show the motion of the Weyl points with decreasing θ. At $\theta = 180°$ (collinear case), the two charge-2 Weyl nodes lie on the C_{4z}-protected k_z axis. For $\theta \neq 180°$, each charge-2 Weyl node splits into two charge-1 Weyl nodes which, in turn, move away from the k_z axis. The integer above each Weyl node denotes the chiral charge.

In order to investigate this scenario, we have studied the evolution of the Weyl points upon rotation of all magnetic moments of the Mn$_I$ atoms at the Wyckoff positions $2b$ with respect to the crystallographic z axis by the angle θ, $\boldsymbol{\mu}^{2b} = \mu^{2b}(-\sin\theta\hat{x} + \cos\theta\hat{z})$, whereas fixing the direction of the Mn$_{II}$ magnetic moments as shown in Fig. 4(a). Here, $\theta = 180°$ indicates the collinear (001) ferrimagnetism. Using the Wannier functions, we find that, at $\theta = 160°$, the magnitude of the calculated x component of the magnetic moment of the Mn$_I$ atoms is $0.94\mu_B$/Mn in good agreement with the corresponding experimental values of $1.19\mu_B$. Table III summarizes the comparison of the values of the magnetic moments of the Mn$_I$ atom between theory and experiment. The magnetic moments from the rotated Wannier approach agree with DFT calculations well. Figure 4(b) shows the evolution of the Weyl nodes as θ changes from 180° to 170° and, finally, to 160°. Initially, at $\theta = 180°$, the two charge-2 Weyl nodes lie on the k_z axis. As θ decreases, each charge-2 Weyl node splits into two charge-1 Weyl nodes which move away from the k_z axis, leading to the emergence of four charge-1 Weyl fermions in the case of noncollinear ferrimagnetism. Our electronic structure calculations of the Fermi arcs on the (100) surface for $\theta = 160°$ show that the noncollinear effect is small on the Fermi arcs in Fig. 3(b), at least, for a small angle.

TABLE III. Comparison of the values of the magnetic moments for the Mn$_I$ atoms for the noncollinear case from theory and experiment. μ_z^{2b} (μ_x^{2b}) denotes the z (x) component of the magnetic moment of Mn$_I$.

Method	μ_z^{2b} (μ_B/Mn)	μ_x^{2b} (μ_B/Mn)	θ (deg)
Rotated Wannier	−2.60	0.94	160
GGA + SOC	−2.65	0.95	160
Experiment [34]	−3.07	1.19	159

IV. DISCUSSION

In this section, we discuss the effect of electron-electron interactions U on the equilibrium lattice constants, magnetic moments, and the topology of the band structure for the collinear magnetic structure. As was alluded earlier, we employed $U = 2.6$ eV for Mn_I atoms and $U = 0$ for the remaining atoms, which were found [38] to give a value for the a lattice constant of 3.91 Å in good agreement with the experimental value. However, as shown in Table I, this is at the expense of a worse agreement for both the lattice parameter c and the z component of the magnetic moment of the Mn^{2b} (Mn_I) atoms. As shown in Fig. 2(a), in the absence of SOC, the presence of U shifts the position of the Weyl nodes (red dots) to higher energies and slightly towards the center of the BZ. Moreover, even in the presence of SOC, the nodes are robust and remain gapless at about the same energies. Therefore, the charge-2 Weyl nodes survive in the presence of electronic correlations. Moreover, since the effect of electronic correlations cannot gap out the charge-2 Weyl nodes, the charge-1 Weyl nodes splitting of the charge-2 Weyl nodes should be robust in the noncollinear magnetic structure as well.

Due to the large shift of the Weyl nodes to higher energies induced by U, it will be challenging to observe the Fermi arcs above the Fermi level in Fig. 3(b) employing angle-resolved photoemission spectroscopy (ARPES). On the other hand, the time-resolved ARPES, a fast-growing and powerful technique to observe conduction electron states up to hundreds of meV above the Fermi level [47,48] may be a suitable platform to observe the Fermi arcs above the Fermi level on the (100) surface in future experiments. Moreover, electron doping or alloying that preserves the C_{4z} symmetry, e.g., $\mathrm{Mn}_3\mathrm{Ge}$ in the cubic structure [18], can rise the chemical potential which may allow, in turn, the observation of these nontrivial surface states emerging from the Weyl nodes.

V. CONCLUSION

To summarize, our *ab initio* electronic structure calculations have shown that, in the absence of SOC, nontrivial nodal lines emerge in collinear ferrimagnetic tetragonal $\mathrm{Mn}_3\mathrm{Ga}$. The nodal lines are protected by both mirror reflection symmetry normal to the [110] direction $M_{[110]}$ and a fourfold rotational symmetry C_{4z}. The presence of SOC gaps out the nodal lines except for the nodal line intersecting points which become C_{4z}-protected charge-2 Weyl nodes with quadratic dispersion on the k_x-k_y plane. The noncollinear magnetism associated with the Mn_I atoms splits the double Weyl node fermions into two charge-1 Weyl nodes moving away from the k_z axis, whose separation can be selectively tuned by the noncollinearity angle.

ACKNOWLEDGMENTS

The work at CSUN was supported by NSF-Partnership in Research and Education in Materials (PREM) Grant No. DMR-1828019. H.L. acknowledges support by the Ministry of Science and Technology (MOST) in Taiwan under Grant No. MOST 109-2112-M-001-014-MY3.

---

[1] P. Tang, Q. Zhou, and S.-C. Zhang, Phys. Rev. Lett. **119**, 206402 (2017).

[2] B.-J. Yang, E.-G. Moon, H. Isobe, and N. Nagaosa, Nat. Phys. **10**, 774 (2014).

[3] N. P. Armitage, E. J. Mele, and A. Vishwanath, Rev. Mod. Phys. **90**, 015001 (2018).

[4] M. Z. Hasan, S.-Y. Xu, and G. Bian, Phys. Scr. **2015**, 014001 (2015).

[5] S.-M. Huang, S.-Y. Xu, I. Belopolski, C.-C. Lee, G. Chang, T.-R. Chang, B. Wang, N. Alidoust, G. Bian, M. Neupane *et al.*, Proc. Natl. Acad. Sci. USA **113**, 1180 (2016).

[6] C. Fang, M. J. Gilbert, X. Dai, and B. A. Bernevig, Phys. Rev. Lett. **108**, 266802 (2012).

[7] Z. Gao, M. Hua, H. Zhang, and X. Zhang, Phys. Rev. B **93**, 205109 (2016).

[8] B. Bradlyn, J. Cano, Z. Wang, M. G. Vergniory, C. Felser, R. J. Cava, and B. A. Bernevig, Science **353**, aaf5037 (2017).

[9] N. Morali, R. Batabyal, P. K. Nag, E. Liu, Q. Xu, Y. Sun, B. Yan, C. Felser, N. Avraham, and H. Beidenkopf, Science **365**, 1286 (2019).

[10] I. Belopolski, T. A. Cochran, S. S. Tsirkin, Z. Guguchia, J. Yin, S. S. Zhang, Z. Cheng, X. Liu, G. Chang, X. Yang *et al.*, arXiv:2005.02400.

[11] I. Belopolski, K. Manna, D. S. Sanchez, G. Chang, B. Ernst, J. Yin, S. S. Zhang, T. Cochran, N. Shumiya, H. Zheng *et al.*, Science **365**, 1278 (2019).

[12] C. Felser and A. Hirohata, *Heusler Alloys Properties, Growth, Applications* (Springer, Cham, 2015).

[13] J. Winterlik, S. Chadov, A. Gupta, V. Alijani, T. Gasi, K. Filsinger, B. Balke, G. H. Fecher, C. A. Jenkins, F. Casper *et al.*, Adv. Mater. **24**, 6283 (2012).

[14] R. A. de Groot, F. M. Mueller, P. G. van Engen, and K. H. J. Buschow, Phys. Rev. Lett. **50**, 2024 (1983).

[15] S. Chadov, X. Qi, J. Kübler, G. H. Fecher, C. Felser, and S. C. Zhang, Nat. Mater. **9**, 541 (2010).

[16] H. Lin, L. A. Wray, Y. Xia, S. Xu, S. Jia, R. J. Cava, A. Bansil, and M. Z. Hasan, Nat. Mater. **9**, 546 (2010).

[17] K. Cai, Z. Zhu, J. M. Lee, R. Mishra, L. Ren, S. D. Pollard, P. He, G. Liang, K. L. Teo, and H. Yang, Nat. Electron. **3**, 37 (2020).

[18] D. Zhang, B. Yan, S.-C. Wu, J. Kübler, G. Kreiner, S. S. P. Parkin, and C. Felser, J. Phys.: Condens. Matter **25**, 206006 (2013).

[19] S. Khmelevskyi, A. V. Ruban, and P. Mohn, Phys. Rev. B **93**, 184404 (2016).

[20] N. Kiyohara, T. Tomita, and S. Nakatsuji, Phys. Rev. Appl. **5**, 064009 (2016).

[21] A. K. Nayak, J. E. Fischer, Y. Sun, B. Yan, J. Karel, A. C. Komarek, C. Shekhar, N. Kumar, W. Schnelle, J. Kübler *et al.*, Sci. Adv. **2**, e1501870 (2016).

[22] H. Yang, Y. Sun, Y. Zhang, W.-J. Shi, S. S. P. Parkin, and B. Yan, New J. Phys. **19**, 015008 (2017).

[23] K. Kuroda, T. Tomita, M.-T. Suzuki, C. Bareille, A. A. Nugroho, P. Goswami, M. Ochi, M. Ikhlas, M. Nakayama, S. Akebi *et al.*, Nature Mater. **16**, 1090 (2017).

[24] Z. H. Liu, Y. J. Zhang, G. D. Liu, B. Ding, E. K. Liu, H. M. Jafri, Z. P. Hou, W. H. Wang, X. Q. Ma, and G. H. Wu, Sci. Rep. **7**, 515 (2017).

[25] E. Liu, Y. Sun, N. Kumar, L. Muechler, A. Sun, L. Jiao, S.-Y. Yang, D. Liu, A. Liang, Q. Xu *et al.*, Nat. Phys. **14**, 1125 (2018).

[26] P. K. Rout, P. V. P. Madduri, S. K. Manna, and A. K. Nayak, Phys. Rev. B **99**, 094430 (2019).

[27] F. Wu, S. Mizukami, D. Watanabe, H. Naganuma, M. Oogane, Y. Ando, and T. Miyazaki, Appl. Phys. Lett. **94**, 122503 (2009).

[28] Z. Bai, Y. Cai, L. Shen, M. Yang, V. Ko, G. Han, and Y. Feng, Appl. Phys. Lett. **100**, 022408 (2012).

[29] S. Mizukami, F. Wu, A. Sakuma, J. Walowski, D. Watanabe, T. Kubota, X. Zhang, H. Naganuma, M. Oogane, Y. Ando *et al.*, Phys. Rev. Lett. **106**, 117201 (2011).

[30] H. Kurt, K. Rode, M. Venkatesan, P. Stamenov, and J. M. D. Coey, Phys. Rev. B **83**, 020405(R) (2011).

[31] J. Winterlik, B. Balke, G. H. Fecher, C. Felser, M. C. M. Alves, F. Bernardi, and J. Morais, Phys. Rev. B **77**, 054406 (2008).

[32] E. Krén and G. Kádár, Solid State Commun. **8**, 1653 (1970).

[33] Q. Sun, S. Kwon, M. Stamenova, S. Sanvito, and N. Kioussis, Phys. Rev. B **101**, 134419 (2020).

[34] K. Rode, N. Baadji, D. Betto, Y.-C. Lau, H. Kurt, M. Venkatesan, P. Stamenov, S. Sanvito, J. M. D. Coey, E. Fonda *et al.*, Phys. Rev. B **87**, 184429 (2013).

[35] G. Kresse and J. Hafner, Phys. Rev. B **48**, 13115 (1993).

[36] J. P. Perdew, K. Burke, and M. Ernzerhof, Phys. Rev. Lett. **77**, 3865 (1996).

[37] S. L. Dudarev, G. A. Botton, S. Y. Savrasov, C. J. Humphreys, and A. P. Sutton, Phys. Rev. B **57**, 1505 (1998).

[38] S. K. Saha, Z. Liu, and G. Dutta, Sci. Rep. **7**, 13221 (2017).

[39] D. D. Koelling and B. N. Harmon, J. Phys. C: Solid State Phys. **10**, 3107 (1977).

[40] A. A. Mosto, J. R. Yates, G. Pizzi, Y.-S. Lee, I. Souza, D. Vanderbilt, and N. Marzari, Comput. Phys. Commun. **178**, 685 (2008).

[41] B. Balke, G. H. Fecher, J. Winterlik, and C. Felser, Appl. Phys. Lett. **90**, 152504 (2007).

[42] N. Al-Aqtash and R. Sabrianov, J. Magn. Magn. Mater. **391**, 26 (2015).

[43] R. Yu, X. L. Qi, A. Bernevig, Z. Fang, and X. Dai, Phys. Rev. B **84**, 075119 (2011).

[44] C.-K. Chiu and A. P. Schnyder, Phys. Rev. B **90**, 205136 (2014).

[45] C. Fang, Y. Chen, H.-Y. Kee, and L. Fu, Phys. Rev. B **92**, 081201(R) (2015).

[46] Our GGA $+ U +$ SOC electronic structure calculations reveal that the Weyl nodes are robust and remain gapless even in the presence of U.

[47] J. A. Sobota, S. Yang, J. G. Analytis, Y. L. Chen, I. R. Fisher, P. S. Kirchmann, and Z.-X. Shen, Phys. Rev. Lett. **108**, 117403 (2012).

[48] H. Soifer, A. Gauthier, A. F. Kemper, C. R. Rotundu, S.-L. Yang, H. Xiong, D. Lu, M. Hashimoto, P. S. Kirchmann, J. A. Sobota, and Z.-X. Shen, Phys. Rev. Lett. **122**, 167401 (2019).